Low-Frequency Variability of Monsoon-Driven Circulation with Application to the South China Sea

HAIYUAN YANG AND LIXIN WU

Physical Oceanography Laboratory, and Qingdao Collaborative Innovation Center of Marine Science and Technology, Ocean University of China, Qingdao, China

SUN SHANTONG

Scripps Institution of Oceanography, University of California, San Diego, La Jolla, California

CHEN ZHAOHUI

Physical Oceanography Laboratory, and Qingdao Collaborative Innovation Center of Marine Science and Technology, Ocean University of China, Qingdao, China

(Manuscript received 16 October 2014, in final form 25 March 2015)

ABSTRACT

The interannual variability of the upper-ocean circulation forced by seasonally varying monsoonal wind is investigated in a two-layer quasigeostrophic (QG) model, with the aim to understand the low-frequency variability of the South China Sea (SCS) circulation. It is demonstrated that the seasonally varying monsoonal wind can force the upper-ocean circulation with significant internal variability, which is mainly associated with the intrinsic nonlinear dynamics of the summer double-gyre system. This arises from the fact that the intrinsic variability, characterized by the Rossby wave adjustment in the winter single-gyre system, is much weaker than that in the summer double-gyre system driven by the intergyre eddy potential vorticity flux through barotropic instability.

1. Introduction

As the largest marginal sea in the Southeast Asian monsoon region, the South China Sea (SCS) has a deep, semienclosed basin with an area of about $3.5 \times 10^6\,\mathrm{km}^2$ (Fig. 1a). Driven by monsoonal wind, the surface circulation in the SCS presents a basin-scale, cyclonic pattern in winter and a double-gyre structure in summer (Wyrtki 1961; Fang et al. 1998; Hu et al. 2000; Liu et al. 2008; Wang et al. 2013). Subsequent studies indicated that the seasonal variability of the SCS circulation is subjected to the quasi-steady Sverdrup balance, after a fast adjustment associated with the first-order baroclinic Rossby waves (Liu et al. 2001; Wang et al. 2003). Besides seasonal variation, the upper-ocean circulation in the SCS varies on longer time scales as well. Based on modeling results, variation of the upper-layer circulation in the SCS associated with ENSO was detected (Wu et al. 1998; Xie et al. 2003; Liu et al. 2004; Wu and Chang 2005; C. Wang et al. 2006; Y. G. Wang et al. 2006; Chang et al. 2008; Liu et al. 2011; Li et al. 2014; Chen and Wang 2014). By combining different observational and assimilative data, Fang et al. (2006) and Yang and Wu (2012) estimated the trend of the surface circulation, wind, SST, and SSH. These studies indicate a potential role of the interannual monsoon variability in regulating the SCS circulation. However, it remains elusive whether the seasonally varying monsoon itself can induce interannual variability in the SCS, given the fast linear wave adjustment at seasonal time scales in the SCS.

In the open oceans, previous studies have highlighted the role of nonlinear adjustment in regulating the ocean on interannual/decadal time scales under steady wind forcing. Based on model results, variability generated through intrinsic ocean dynamics was recognized by Bryan (1963) and Holland (1978). After their work, different variations and their mechanisms have been discussed with idealized models. Since the 1990s, it was found that the ocean variability can be understood through bifurcations of nonlinear dynamical systems (e.g., Cessi and Ierley

Corresponding author address: Haiyuan Yang, Physical Oceanography Laboratory, Ocean University of China, 238 Songling Road, Qingdao 266100, China.
E-mail: yanghaiyuan@ouc.edu.cn

DOI: 10.1175/JPO-D-14-0212.1

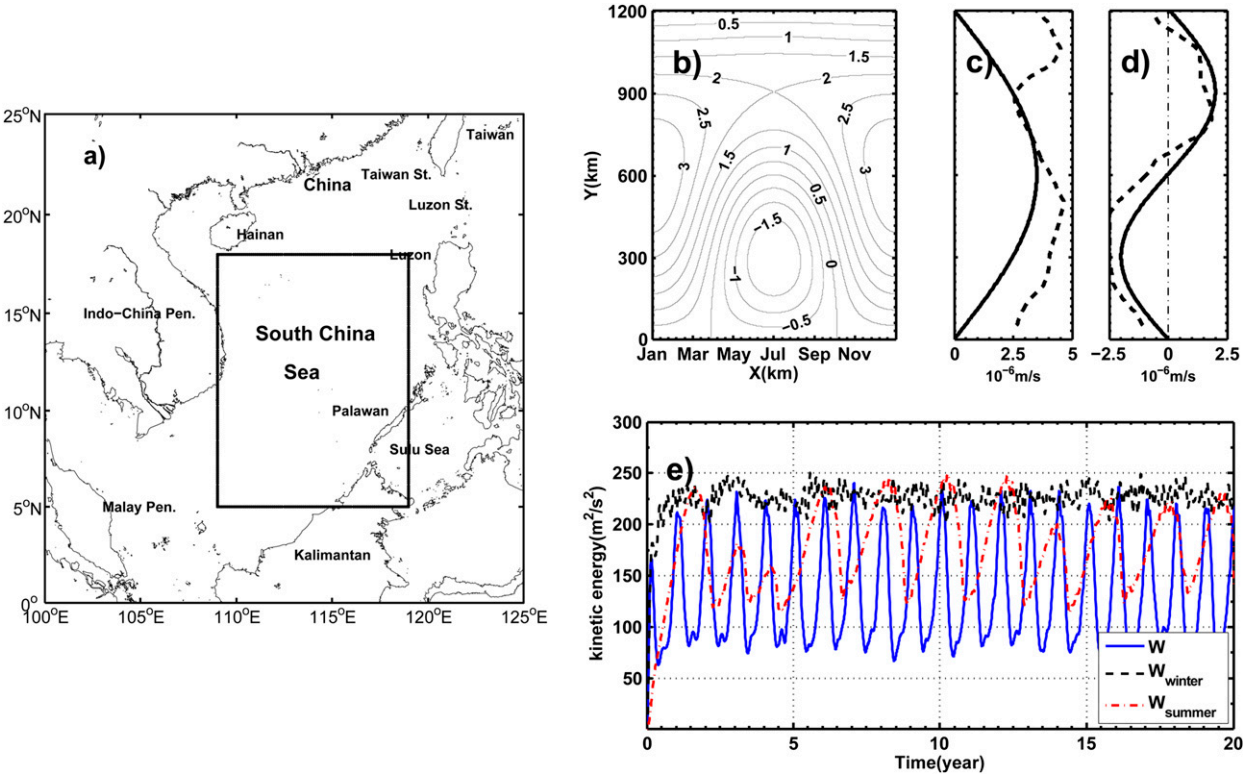

FIG. 1. (a) Map of the South China Sea. The domain of integration is shown as a black rectangle. (b) Temporal and meridional structure of Ekman pumping velocity W (10^{-6} m s^{-1}). (c) Meridional patterns for W_1 (solid) and zonal-mean Ekman pumping velocity in December derived from SODA (dashed). (d) Meridional patterns for W_2 (solid) and zonal-mean Ekman pumping velocity in July derived from SODA (dashed). (e) Spinup processes for W-forcing case (blue), W_{winter}-forcing case (black), and W_{summer}-forcing case (red).

1995; Jiang et al. 1995; Meacham and Berloff 1997a,b; Berloff and Meacham 1997, 1998; Qiu and Miao 2000; Primeau 2002; Simonnet et al. 2003; Dijkstra and Ghil 2005; Pierini et al. 2009; Penduff et al. 2011; Pierini et al. 2014). According to this theory, the ocean is characterized by unstable attractors such as fixed points, limit cycles, tori, strange attractors, and homoclinic orbits. On the other hand, studies showed the role of eddy–mean flow interaction in maintaining the gyre circulation and driving the low-frequency variability (McCalpin and Haidvogel 1996; Berloff 2005; Berloff et al. 2007a,b). For example, McCalpin and Haidvogel (1996) concluded that the low-frequency variability associated with their double gyre is caused by the eddy–flow interaction in the jet exit region in a quasigeostrophic (QG) model. Berloff et al. (2007a) reported a turbulent phenomenon, which is characterized by changes in the meridional position and strength of the oceanic eastward jet (EJ), driven by the competition between the eddy rectification process and potential vorticity (PV) anomaly induced by intergyre transport. In the SCS, nonlinearity is found to be important in the seasonal establishment of the circulation (G. H. Wang et al. 2006), but its role at longer time scales need to be further investigated.

In this paper, the interannual variability of upper-layer circulation in the SCS driven by seasonally varying wind is studied in a two-layer QG model. Using the same model, Mu et al. (2011) studied the low-frequency variability of the Kuroshio intrusion into SCS. Here, we will focus on the variability of the upper-ocean circulation purely induced by seasonal wind, while the effects from the Luzon Strait and the shape/topography of the basin will not be considered. To validate the results from the QG model, data from the Ocean General Circulation Model (OGCM) for the Earth Simulator (OFES) climatological run and Simple Ocean Data Assimilation (SODA) reanalysis product are also analyzed. This paper is organized as follows: Section 2 gives a brief description of QG model, OFES, and SODA. In section 3, detailed examination of model results are presented, followed by discussion and conclusions in section 4.

2. Model

a. QG model

In this study, the numerical experiments are performed based on a two-layer QG model, whose governing equations are as follows (Pedlosky 1987):

$$\frac{\partial q_1}{\partial t} + J(\psi_1, q_1) = \frac{f_0}{H_1} W + A_H \nabla^4 \psi_1, \quad \text{and} \tag{1a}$$

$$\frac{\partial q_2}{\partial t} + J(\psi_2, q_2) = A_H \nabla^4 \psi_2 - \gamma \nabla^2 \psi_2 . \tag{1b}$$

Here, q_i represents the PV, ψ_i is the streamfunction, and H_i is the mean layer thickness, where i ($i = 1, 2$) is the layer index starting from the top. Considering the mean depth of the SCS basin (2000 m) and maximum thermocline depth (Chu et al. 1999), we set $H_1 = 200$ m and $H_2 = 1800$ m. The symbol ∇^2 is the horizontal Laplacian operator and $J(a, b) = a_x b_y - a_y b_x$ is the Jacobian operator; A_H is the horizontal eddy viscosity coefficient and γ is the linear bottom friction coefficient. PV q_i are related to ψ_i through the coupled elliptic equations:

$$q_1 = \nabla^2 \psi_1 + \frac{f_0^2}{g' H_1}(\psi_2 - \psi_1) + \beta y, \quad \text{and} \tag{2a}$$

$$q_2 = \nabla^2 \psi_2 + \frac{f_0^2}{g' H_2}(\psi_1 - \psi_2) + \beta y, \tag{2b}$$

where $g' = g(\rho_2 - \rho_1)/\rho_0$ represents the reduced gravity, g is the gravitational constant, and ρ_0 and ρ_i indicate the reference density and the density of layer i, respectively. Following the work of Liu et al. (2001), we set $g' = 0.03\ \mathrm{m\,s^{-2}}$ in this study. The constant Coriolis parameter is $f_0 = 2.5 \times 10^{-5}\ \mathrm{s^{-1}}$ and $\beta = 2.25 \times 10^{-11}\ \mathrm{m^{-1}\,s^{-1}}$. The model domain is set to a closed rectangle with a size of 1000 and 1200 km in the zonal and meridional directions, which represents a domain covering 5°–17°N, 109°–119°E (Fig. 1a).

In this study, the model is driven by vertical Ekman pumping velocity. The seasonal-varying forcing W (Fig. 1b) consists of a single-gyre component W_1 and a double-gyre component W_2:

$$W = \frac{(W_1 - W_2)}{2}\cos(2\pi\Omega t) + \frac{(W_1 + W_2)}{2}, \tag{3a}$$

$$W_1 = w_1 \sin\left(\frac{\pi}{L_y} y\right), \quad \text{and} \tag{3b}$$

$$W_2 = w_2 \sin\left(-\frac{2\pi}{L_y} y\right). \tag{3c}$$

Here, W_2 is prescribed in an antisymmetric form with respect to the midbasin axis, while W_1 is characterized by a single-gyre pattern with its maximum located at the midbasin, representing a crude model of the SCS monsoon in July and December (Figs. 1c,d). The term Ω is frequency with the value of $1\ \mathrm{yr^{-1}}$. In addition to W (W-forcing case), the SCS will also be driven by steady winter/summer monsoon ($W_{\mathrm{winter}}/W_{\mathrm{summer}}$-forcing case), which is defined as the time-mean W during December–February/June–August. Under this setting, W_{summer} is set to be slightly asymmetric with respect to the midbasin in order to avoid the artificial symmetrization of the gyres in the turbulent regime (Berloff and McWilliams 1999).

TABLE 1. The reference parameters used in the model.

Model parameters			
H_1	200 m	H_2	1800 m
L_x	1000 km	L_y	1200 km
ρ_0	$1000\ \mathrm{kg\,m^{-3}}$	g'	$0.03\ \mathrm{m\,s^{-2}}$
f_0	$2.5 \times 10^{-5}\ \mathrm{s^{-1}}$	β	$2.25 \times 10^{-11}\ \mathrm{m^{-1}\,s^{-1}}$
A_H	$150\ \mathrm{m^2\,s^{-1}}$	γ	$10^{-7}\ \mathrm{m\,s^{-1}}$
w_1	$3.5 \times 10^{-6}\ \mathrm{m\,s^{-1}}$	w_2	$2 \times 10^{-6}\ \mathrm{m\,s^{-1}}$
α	$0.1\ \mathrm{km^{-1}}$	δ_s	5 km
δ_t	1800 s		

The boundary conditions used here are no normal flow condition,

$$\psi_i = \psi_i(t), \tag{4}$$

and partial-slip lateral boundary condition (Haidvogel et al.1992),

$$\frac{\partial^2 \psi_i}{\partial n^2} - \alpha \frac{\partial \psi_i}{\partial n} = 0, \tag{5}$$

where n is the direction normal to the lateral boundary and oriented outwardly. In the reference case, $\alpha = 0.1\ \mathrm{km^{-1}}$ lies between the no-slip lateral boundary condition ($\alpha \to \infty$) and the free-slip boundary condition ($\alpha = 0$). In addition, the mass conservation equation (McWilliams 1977)

$$\frac{\partial}{\partial t} \iint (\psi_1 - \psi_2)\, ds = 0 \tag{6}$$

is also adopted.

The reference parameters used in the model are listed in Table 1. The spatial resolution is 5 km, which can resolve mesoscale eddies. Under this parameter setting, the Munk length scale $\delta_M = (A_H/\beta)^{1/3}$ is 18.8 km, and the baroclinic deformation radius $R_d = \sqrt{g' H_1 H_2/(H_1 + H_2)}/f_0$ is 92.9 km, which cover 3 and 18 grid points, respectively. The wave speed of the first baroclinic long Rossby wave $C_R = \beta R_d^2$ is $20\ \mathrm{cm\,s^{-1}}$, which is within the former estimations in the middle SCS [10–40 $\mathrm{cm\,s^{-1}}$ in Liu et al. (2001)]. Considering the basin width $L = 1000$ km, transit time across the basin for first-order baroclinic Rossby waves is 57 days, which is much shorter than 1 yr. In each case, the model is first integrated using a leapfrog time-stepping algorithm from rest to steady state judged by the total kinetic energy (Fig. 1e). After the spinup, each case is integrated for another 16 yr, and the results are stored at 5-day intervals for analysis. For a more detailed setting of this model, readers are referred to Mu et al. (2011) and Sun et al. (2013).

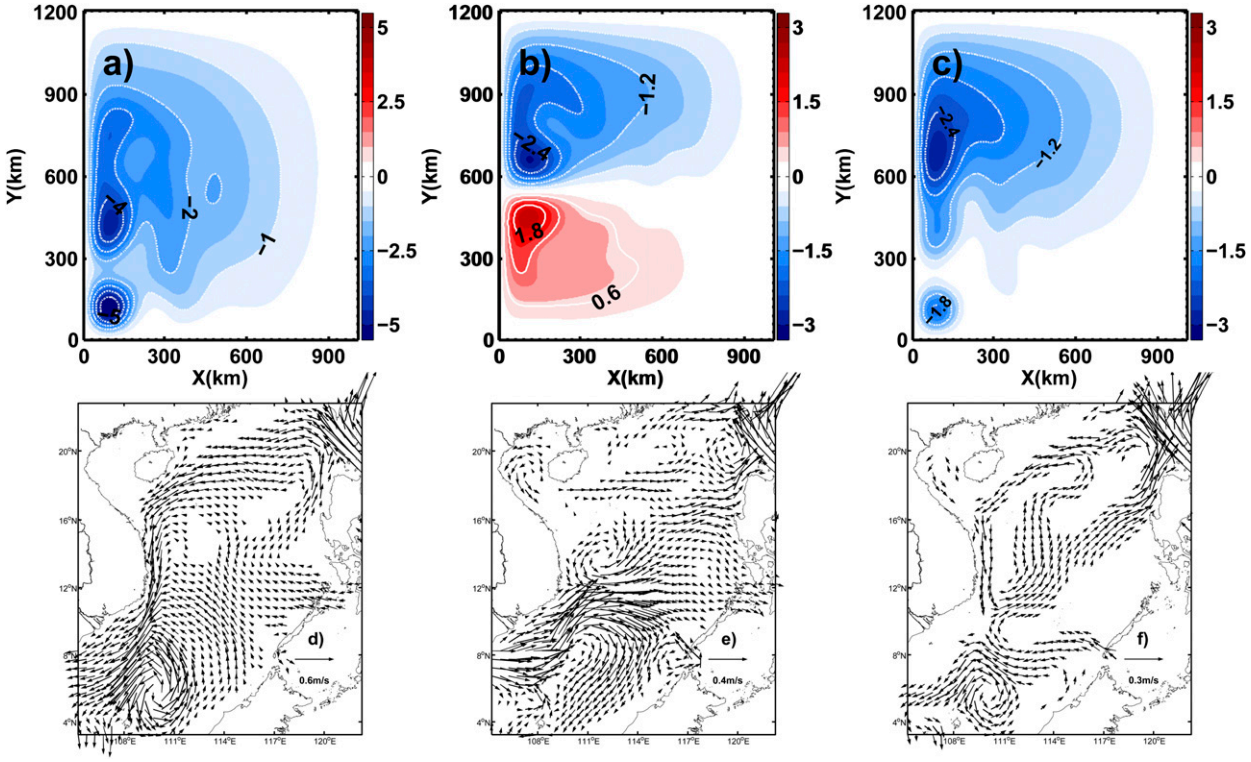

FIG. 2. QG model-simulated SCS (a) winter-mean, (b) summer-mean, and (c) annual-mean upper-layer dynamical streamfunction (Sv). (d) Winter-mean, (e) summer-mean, and (f) annual-mean surface velocity field derived from SODA.

b. *SODA reanalysis product*

To validate the results from QG model, monthly mean data from the SODA 2.0.2/2.0.4 product (Carton et al. 2000, 2005) is used in this study. It is created by the Parallel Ocean Program (POP) ocean model with an average horizontal resolution of 0.5° × 0.5° and 40 levels in the vertical. The model is forced by the European Centre for Medium-Range Weather Forecasts (ECMWF) ERA-40 reanalysis wind stresses from 1958 to 2001 and incorporates virtually all available hydrographic profile data, as well as ocean station data, moored temperature and salinity time series, surface temperature and salinity observations of various types, and nighttime infrared satellite SST data during the assimilation. Assimilation of observations and reanalysis data is carried out sequentially using random continuous estimation theory and quality control methods, for example, the ''forecasting–observation'' test, Kalman filter, and four-dimensional variational data assimilation (4-DVar) to reduce the system errors. Here, the monthly data from 1993 to 2008 and a domain covering 108.25°–121.25°E, 3.25°–22.25°N are analyzed.

c. *OFES model data*

To further validate the intrinsic variability of the SCS from the QG model, the SSH field derived from the high-resolution OFES is also analyzed (Sasaki et al. 2004, 2007). The model is based on the Modular Ocean Model (MOM3), with a near-global domain extending from 75°S to 75°N and a horizontal resolution of 0.1° × 0.1°. There are 54 levels in the vertical direction with increasing thickness ranging from 5 m near the sea surface to 330 m at 6065 m. Initialized at rest with annual-mean temperature and salinity fields of the *World Ocean Atlas 1998* (*WOA98*), the model is run for 50 yr with monthly climatological forcing surface fluxes derived from the National Centers for Environmental Prediction–National Center for Atmospheric Research (NCEP–NCAR) reanalysis for 1950–99. In this study, monthly output in the final 10 model years (41–50) and a domain covering (5°–20°N, 108°–120°E) is used.

3. Results

a. *Interannual variability of the SCS upper-layer circulation*

The time-averaged, upper-layer circulations forced by W are plotted in Figs. 2a–c for the winter, summer, and annual means, respectively. In winter, a basin-scale cyclonic circulation occupies the entire SCS basin (Fig. 2a). A well-developed southward current extends along the

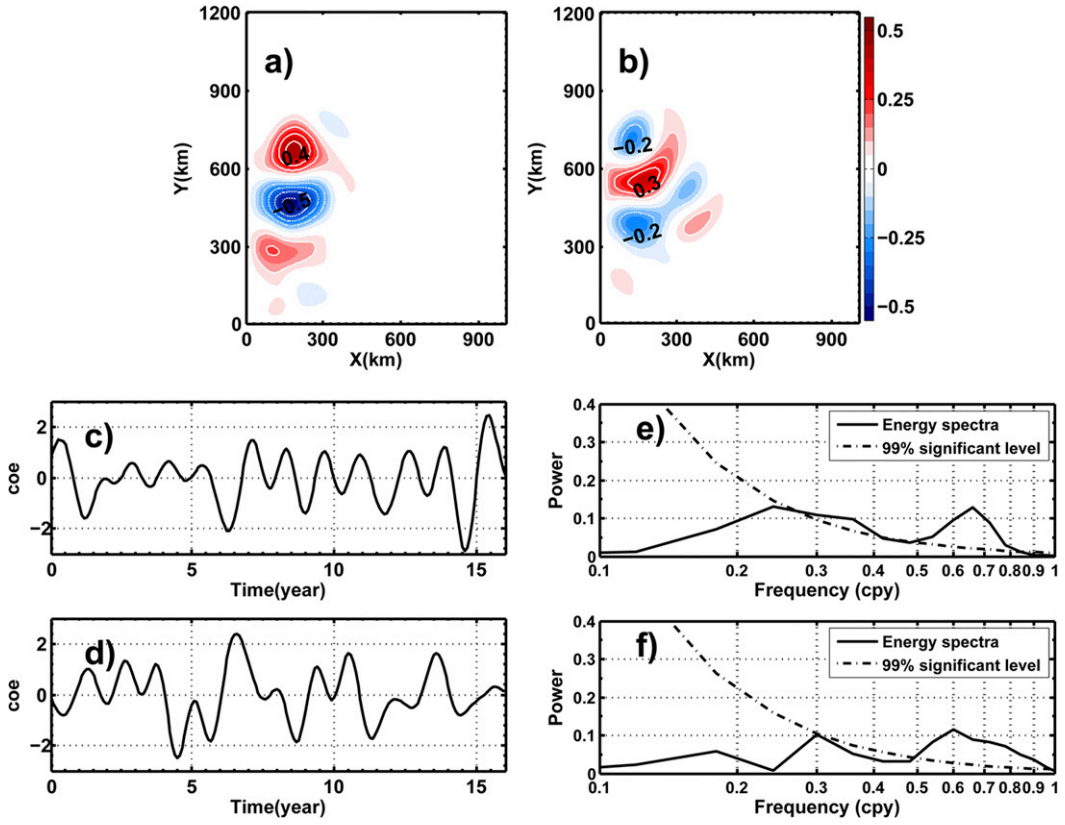

FIG. 3. (a) First and (b) second EOF modes of for I-band streamfunction (Sv). (c),(d) Their corresponding PCs with (e),(f) energy spectra.

western boundary where a recirculation [northern recirculation (NR)] with transport around 4.5 Sverdrups (Sv; $1\,\text{Sv} \equiv 10^6\,\text{m}^3\,\text{s}^{-1}$) can be detected, while the southwestern corner of the basin is dominated by a stronger recirculation gyre [main recirculation (MR)] with a transport of 5.5 Sv. In summer, the circulation is characterized by a double-gyre pattern (Fig. 2b). An EJ is located between these two gyres with transport around 5 Sv. The annual-mean circulation shows a similar pattern with that in winter but has a much weaker transport (Fig. 2c). An EJ induced by the large cyclonic gyre located near the middle basin can also be found. Both the circulation pattern and seasonal evolution are in good agreement with the SODA reanalysis (Figs. 2d–f). In the following, we will assess the interannual variability.

To extract the dominant patterns of variability, the empirical orthogonal function (EOF) method is used. As we focus on the interannual time scale, the seasonal and decadal cycle of the circulation is first removed through bandpass filtering between 400 day and 8 yr (I band). The leading EOF pair (Figs. 3a,b) contains about 50% (32.7% and 17.8%) of the total variance and represents a coherent pattern in the midbasin near the western boundary with the prime frequency around $0.6\,\text{yr}^{-1}$ (Figs. 3e,f). The first mode shows a peak at 0.5 Sv with a quasi-dipolar structure antisymmetric with respect to the midbasin axis, while the second mode is characterized by a tripolar pattern with amplitude around 0.3 Sv. The correlation between them is −0.25/0.25 (exceeding the 99% confidence level) when the first mode leads/lags the second mode by about 5 months (not shown), suggesting a periodic cycle consists of these two modes. Another interesting feature in Figs. 3e and 3f is that both modes have secondary frequencies around $0.2–0.3\,\text{yr}^{-1}$ that may be caused by the bifurcation associated with nonlinear terms. As these frequencies are insignificant and cannot be found in OFES (Fig. 17), we will not discuss them in this study.

To better understand the interannual modes, EOF is also performed to analyze the wintertime and summertime of the upper-layer SCS. Figures 4a and 4b show the structure of the leading EOF pair for wintertime, which account for 29.0% and 19.2% of the total variance. The first mode shows a zonal wavelike structure, while the second mode is characterized by a meridional one. Unlike those in wintertime, the first two EOF modes for summertime (Figs. 4c,d) present

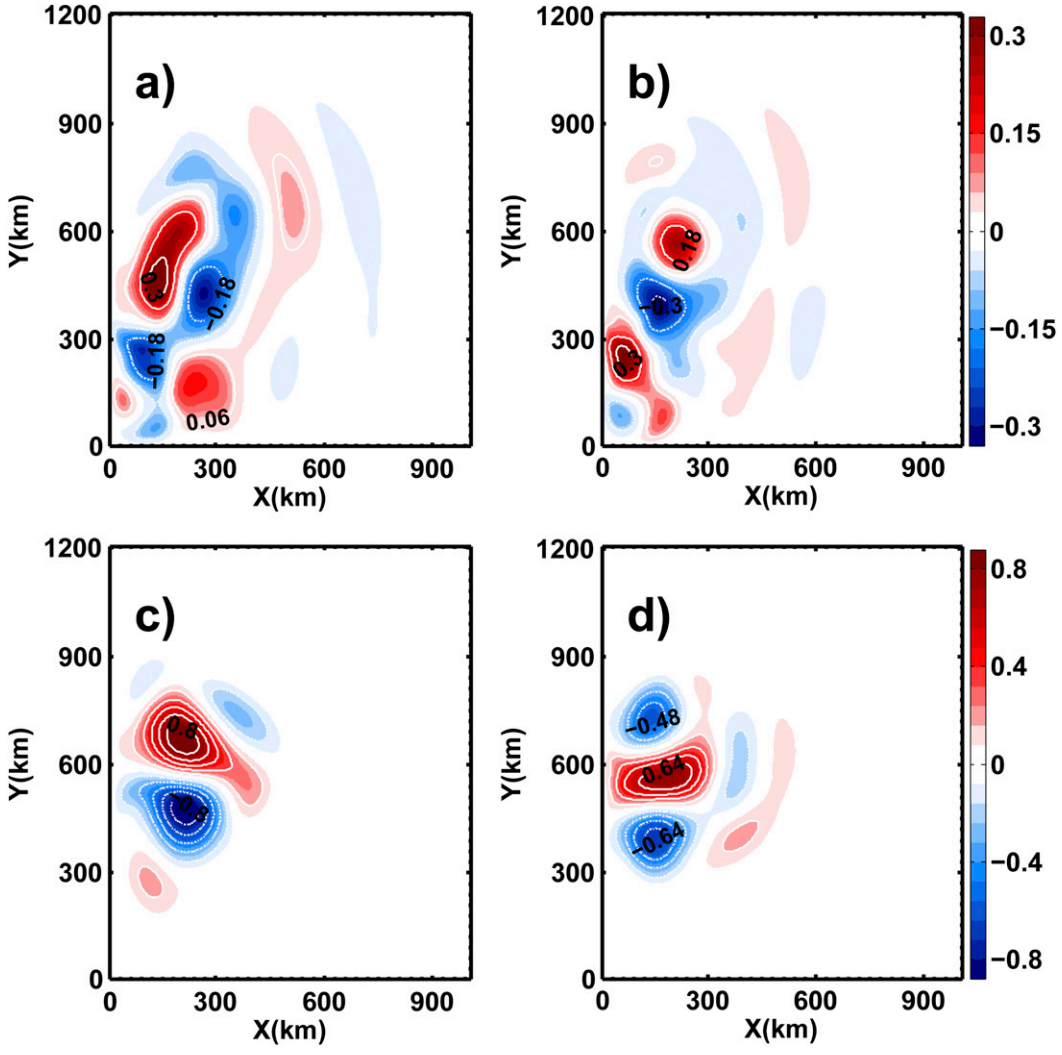

FIG. 4. (a) First and (b) second EOF modes for wintertime streamfunction (Sv). (c),(d) As in (a) and (b), but for summertime.

similar structures to Figs. 3a and 3b, characterized by meridional dipole (40.9%) and tripole (29.4%) that are quasi symmetric with respect to the midbasin axis but with much larger amplitude. This consistency is also presented on the standard deviation field of streamfunction (not shown), suggesting that the interannual evolution of the upper-layer SCS may be dominated by the double-gyre system in summer. In the following sections, we will verify this hypothesis by analyzing the intrinsic variability of the SCS under steady forcing.

b. Variability of the SCS forced by W_{winter}

Figure 5a shows the mean upper-layer streamfunction forced by W_{winter}. The circulation presents a cyclonic gyre with the MR developed in the southwestern basin and transport of 5 Sv. Both its pattern and transport resemble those in Fig. 2a, which are mainly because of the fast Rossby wave adjustment. The first two EOF modes for the I-band streamfunction and their frequency spectra are shown in Fig. 6. Variance contributions of the modes are 33.1% and 18.2%, respectively. Spatially, distributions for both of these two modes are characterized by significant signals in the southwestern basin caused by variability associated with the MR and the NR. Frequencies are 0.48 yr^{-1} (Fig. 6e) and 0.38/0.66 yr^{-1} (Fig. 6f) with a correlation of 0.4 when the second mode leads by 13 months.

Is this the intrinsic variability of SCS forced by W_{winter}? To answer this question, we decompose the streamfunction, without time filtering, in the pair of EOFs, which contain 37.3% and 32.7% of the total variance, respectively (Fig. 7). Both of the two modes depict wave

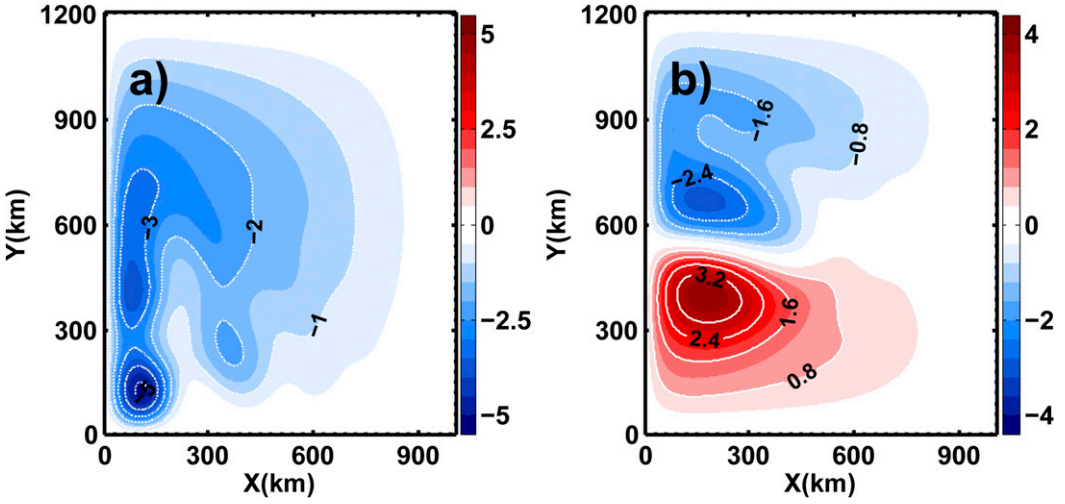

FIG. 5. Mean upper-layer dynamical streamfunction (Sv) derived from the (a) W_{winter}-forcing case and (b) W_{summer}-forcing case.

pattern along the northeastern–southwestern direction with southwestern intensification (Figs. 7a,b) and significant frequency (Figs. 7e,f) of 4 yr^{-1}. Considering the pattern of mean circulation, these modes describe the wave adjustment and variation of the MR area. The magnitude of correlation between them reaches the maximum 0.85 at ±20 days (about one-quarter of the dominant period), suggesting that the signal is nearly periodic.

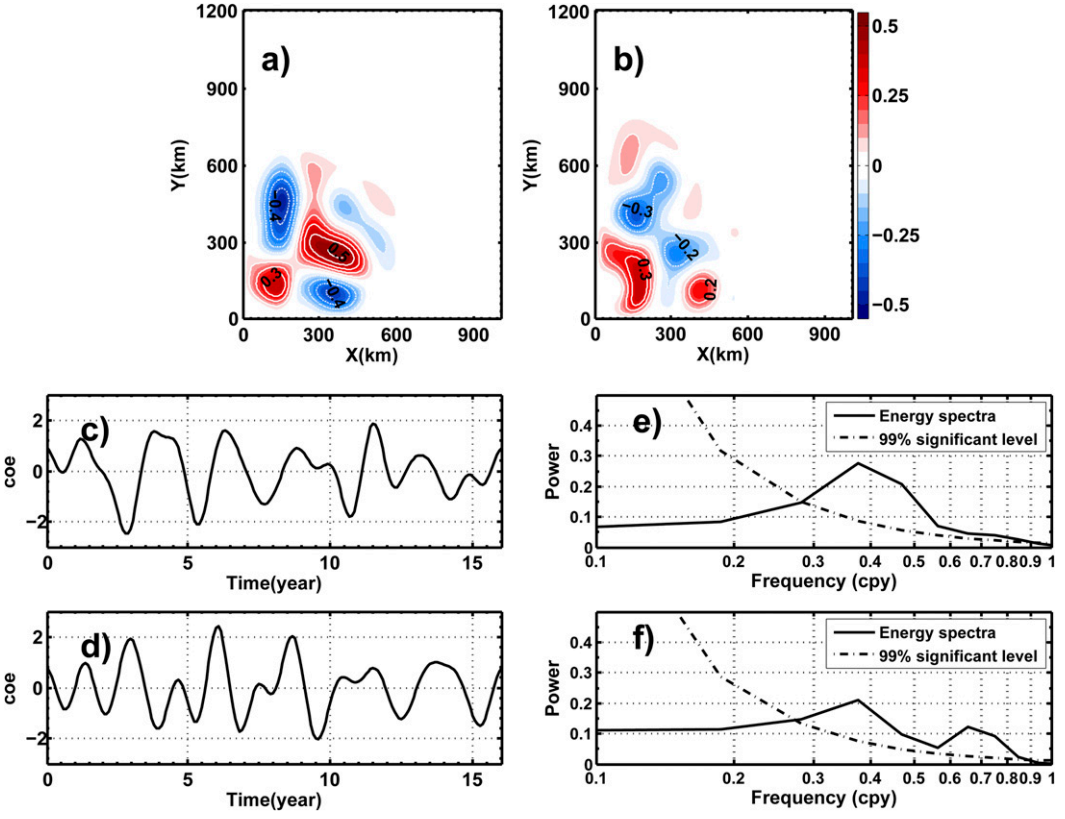

FIG. 6. (a) First and (b) second EOF modes for I-band streamfunction (Sv) for W_{winter}-forcing case. (c),(d) Their corresponding PCs with (e),(f) energy spectra.

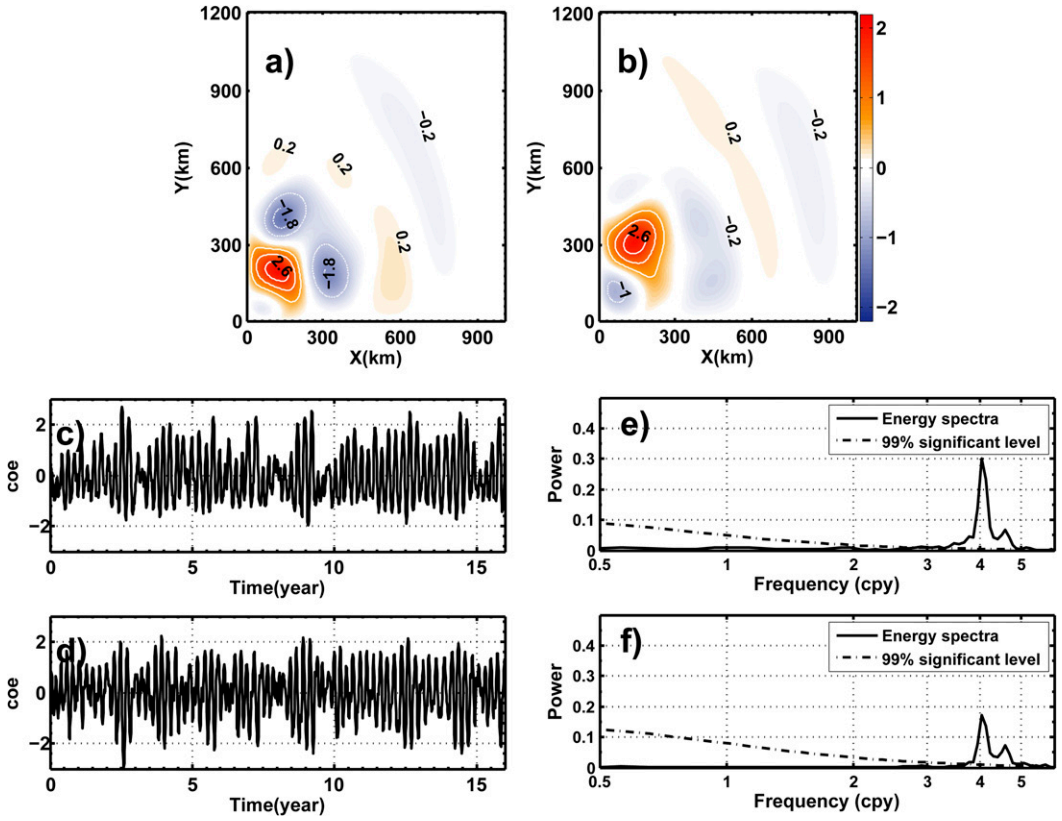

FIG. 7. As in Fig. 6, but for EOF without time filtering.

To explain this intrinsic frequency, we calculate the two-layer Rossby basin mode of the SCS forced by W_{winter} (Cessi and Louazel 2001; Spydell and Cessi 2003). The first eigenvalue is $0.1341 + 4.1681i\,\text{yr}^{-1}$ (close to $4\,\text{yr}^{-1}$) with the associated eigenvector (not shown) similar to that of the EOF modes shown in Fig. 7 and results of Cessi and Louazel (2001, their Fig. 2). Another noticeable feature of this eigenvalue is the positive growth rate, which is different from that in Cessi and Louazel (2001); this may be caused by the resonance between the Rossby wave and nonlinear background circulation. In addition, we also compute this eigenproblem with successively changing resolution on the interval, and the same eigenvalues and eigenvectors are obtained, indicating that calculations used in this paper are robust. To summarize, the consistency between the basin mode and EOF analysis suggests that the intrinsic variability of the single-gyre SCS is dominated by linear Rossby wave adjustment.

c. *Variability of the SCS forced by W_{summer}*

Mean upper-layer streamfunction forced by W_{summer} is shown in Fig. 5b in which a double-gyre pattern is depicted. A strong EJ with transport more than 6 Sv, which is larger compared with that in Fig. 2b, locates to the south of the zero wind curl line between these two gyres. EOF analysis is performed for the I-band model solution. The leading EOF pair (Fig. 8) show the most substantial variability occurs around the EJ with the sense of meridional propagation. Their variance contributions are 51.7% and 44.2%. The first mode (Fig. 8a), which has a tripolar structure, captures the coherent meridional shifts of the jet, while the second mode (Fig. 8b) presents a dipolar structure, describing variations of the intensity of the EJ (e.g., Dewar 2003; Berloff et al. 2007a). Power spectra for both modes are dominated by the peak at $0.54\,\text{yr}^{-1}$ (Figs. 8e,f), which is close to the $0.6\,\text{yr}^{-1}$ frequency in the W-forcing case. Correspondingly, their associated time–lag correlation function is roughly antisymmetric around zero, with the maximum/minimum as $0.9/-0.9$ when the first mode lags/leads about 6 months, indicating a periodic evolution. As in the W_{winter}-forcing case, we perform EOF analysis on the streamfunction without time filtering, and the same results are obtained, suggesting that this interannual variability of the double-gyre system is intrinsic.

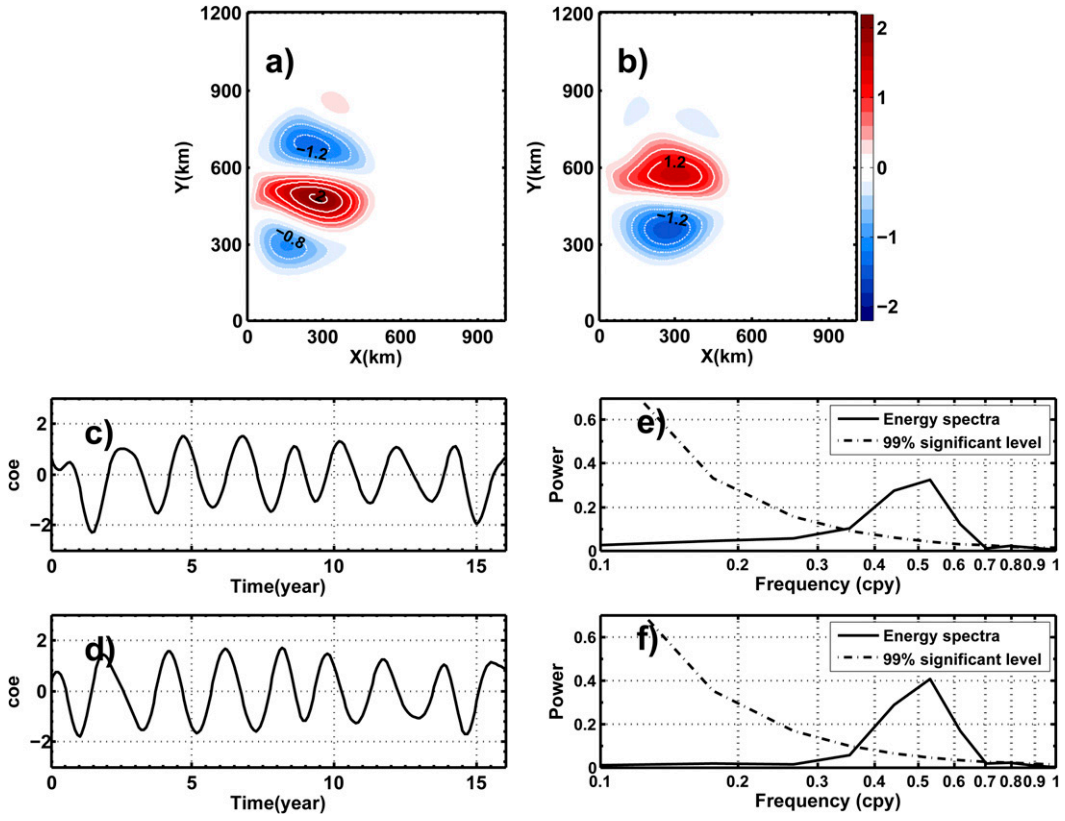

FIG. 8. As in Fig. 6, but for W_{summer}-forcing case.

The two-layer Rossby basin mode for this double-gyre system is also calculated. The frequency of the most unstable mode is 4.2 yr^{-1}, which is much larger than that of intrinsic variability, indicating the importance of the nonlinear term $J(\psi', q')$, which is neglected in the Rossby basin mode, in regulating the SCS circulation. Based on the PV budget associated with $J(\psi', q')$, Berloff et al. (2007a) attributed these variability modes to the PV intergyre transport anomalies within the large Reynolds number regime. In the next section, we will follow their work with the aim of estimating whether this mechanism is suitable for the SCS in which the circulation is much weaker than the open ocean.

Ensemble analysis is used to explore the evolution processes. We first define the ''key states'' of the variability judged by the normalized principal components (PCs) (Fig. 9): States A and B are given by the corresponding ensemble-mean streamfunction in which the PC of the first mode is larger than 1 or less than −1, respectively. States C and D are defined similarly but depend on the amplitude of the second PC. Combined with the time–lag correlation between these two modes, the evolution of the interannual variability can be described in terms of the sequence of transitions: A → D → B → C → A. In state A (Fig. 9a), the EJ shifts to the north with larger transport relative to its time-mean state. The transition process from A to D (Fig. 9d) is characterized by the southward migration of the EJ with slight strengthening. Then the EJ shifts farther southward but begins to weaken in state B (Fig. 9b). After that, the EJ changes its migration direction northward with a substantially weakened transport (Fig. 9c). Finally, the strengthening of the EJ characterizes the transition to state A, and then the cycle repeats itself.

To elucidate the role of each factor in driving the interannual cycle, estimation has been made on the PV budget for the southern gyre (SG) at different states. The PV balance equation is given as follows (Berloff et al. 2007a):

$$\iint_{\Omega} \frac{f_0}{H_1} W \, dS - \int_{\text{EJ}} \boldsymbol{v}' q' \cdot \mathbf{n}_1 \, ds + \int_{\text{EJ}} \mathbf{G}_{\text{diff}} \cdot \mathbf{n}_1 \, ds + \int_{\partial\Omega} \mathbf{G}_{\text{diff}} \cdot \mathbf{n}_2 \, ds = 0. \tag{7}$$

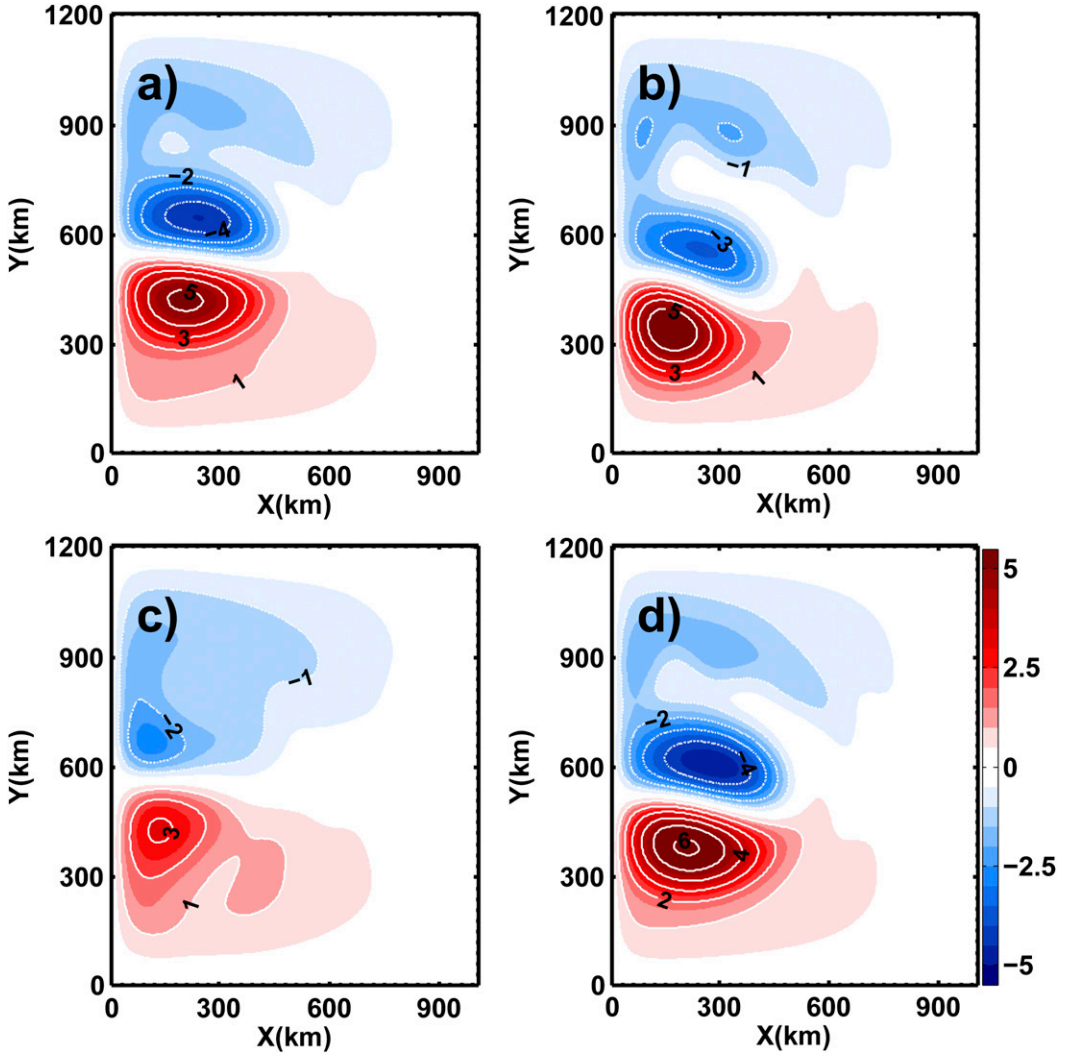

FIG. 9. Ensemble-mean dynamical streamfunctions (Sv) of key states of the interannual mode in W_{summer}-forcing case: (a) A, (b) B, (c) C, and (d) D.

Here $\boldsymbol{v} = (u, v)$ is the horizontal velocity, $\mathbf{G}_{\text{diff}} = -A_H \nabla\nabla^2\psi$ is the diffusive flux of the relative vorticity, and $\mathbf{n}$ is the corresponding normal vector. In Eq. (7), the term on the left-hand side $(f_0/H_1)W$ represents the PV inputs generated by the wind. The term $\boldsymbol{v}'q'$, the product of the perturbation of PV and velocity, represents the horizontal eddy flux. The last two terms represent diffusive flux at the intergyre and basin boundaries, respectively.

PV balance in the SG is summarized in Table 2, in which the budget is characterized by the quasi balance between wind forcing and the diffusive boundary flux, indicating the major PV sources and sinks. Intergyre eddy PV flux is found to be the third major contributor in the PV balance, accounting for around 15% of the former two terms, while the diffusive intergyre flux is negligible. Compared to those in the mean state, roles of these four factors in driving the interannual mode are different. Wind forcing and intergyre eddy PV flux are found to be the major two drivers of the variability, as indicated by their large variances. This resembles the estimations by Berloff et al. (2007a), indicating the importance of the nonlinear term $J(\psi', q')$ in driving the interannual variability.

To obtain a better understanding of the modes, we further estimate the energy exchange between the mean state

TABLE 2. Potential vorticity balances (10^{-4} m^2 s^{-2}) for the upper-layer SCS of SG in the W_{summer}-forcing case.

	A	D	B	C	Mean	Std
Wind input	−792	−775	−772	−795	−784	12
Diffusive boundary flux	656	660	658	650	656	4
Eddy intergyre flux	97	77	101	125	100	20
Diffusive intergyre flux	29	30	28	26	28	2
Total	−10	−8	15	6	0	12

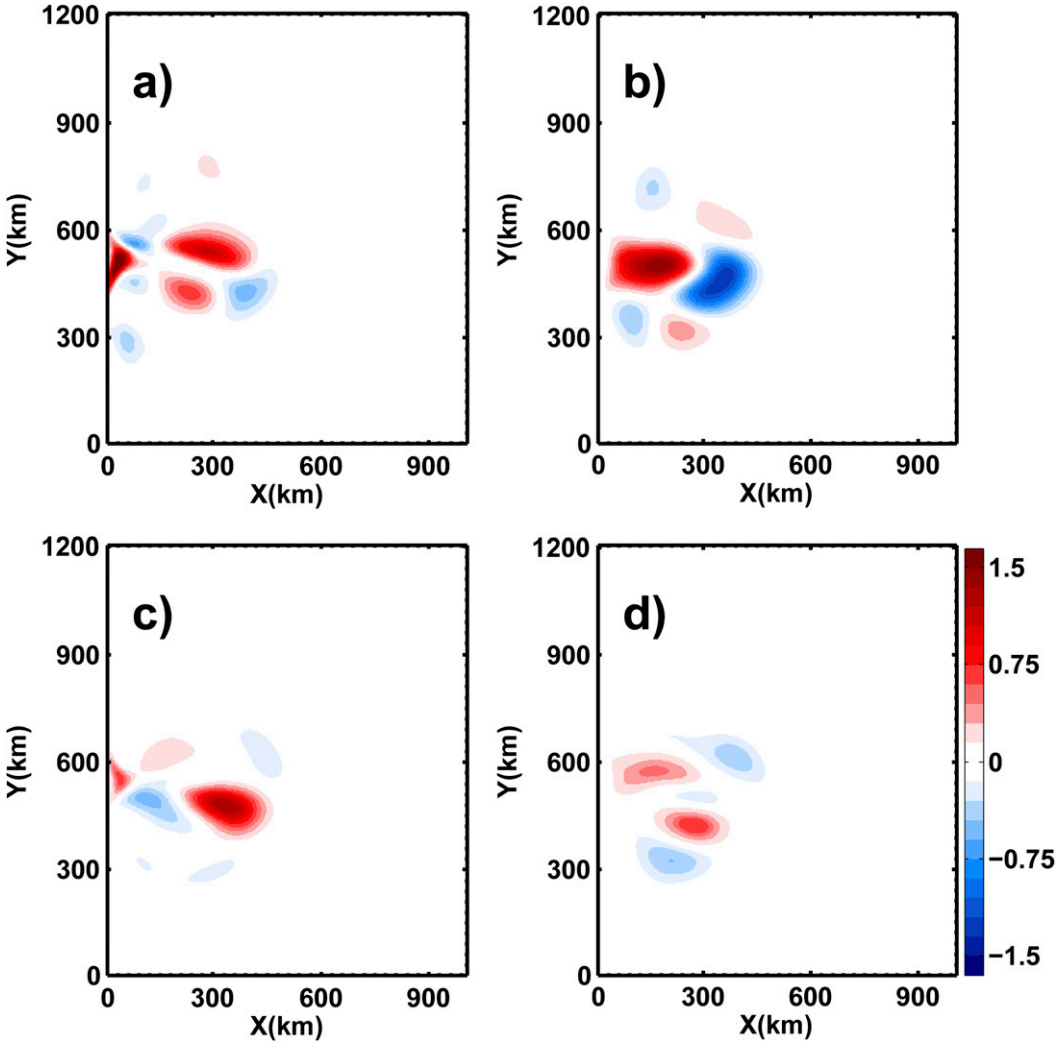

FIG. 10. Energy conversion terms ($10^{-9}\,m^2\,s^{-3}$) (a) P and (b) R associated with the first EOF mode in W_{summer}-forcing case. (c),(d) As in (a) and (b), but for the second mode.

and EOF modes (Berloff and McWilliams 1999) through P, the energy exchange between the mean state and perturbations due to the work done by horizontal Reynolds stress

$$P = -\sum_{k=1,2} \frac{H_k}{H}\left[\frac{\partial \psi_k'}{\partial x} J\left(\psi_k', \frac{\partial \overline{\psi}_k}{\partial x}\right) + \frac{\partial \psi_k'}{\partial y} J\left(\psi_k', \frac{\partial \overline{\psi}_k}{\partial y}\right)\right], \tag{8}$$

and the baroclinic conversion rate R, the energy exchange due to the work done by isopycnal form stress associated with divergence of the heat flux of the fluctuations

$$R = -\frac{f^2}{g'H}(\psi_1' - \psi_2')J(\psi_1' + \psi_2', \overline{\psi}_1 - \overline{\psi}_2). \tag{9}$$

Figure 10 shows the spatial distribution of P and R for the first (Figs. 10a,b) and second (Figs. 10c,d) EOF mode. It is found that both P and R showing western intensification with the most substantial variability around the EJ. Trough barotropic instability modes attain their energy from the mean state at the EJ origin area (Fig. 10a) and the extension area (Fig. 10c), while the spatial distribution of R is characterized by positive values at the EJ upstream area. In Fig. 10b, R depicts negative values at the EJ extension, which is caused by the negative rotational component of buoyancy flux terms (Berloff and McWilliams 1999). Integrating over the whole basin (not shown), it is found that values of P are much larger than that of R for both modes, suggesting that the interannual variability obtains energy from the mean state mainly through barotropic instability.

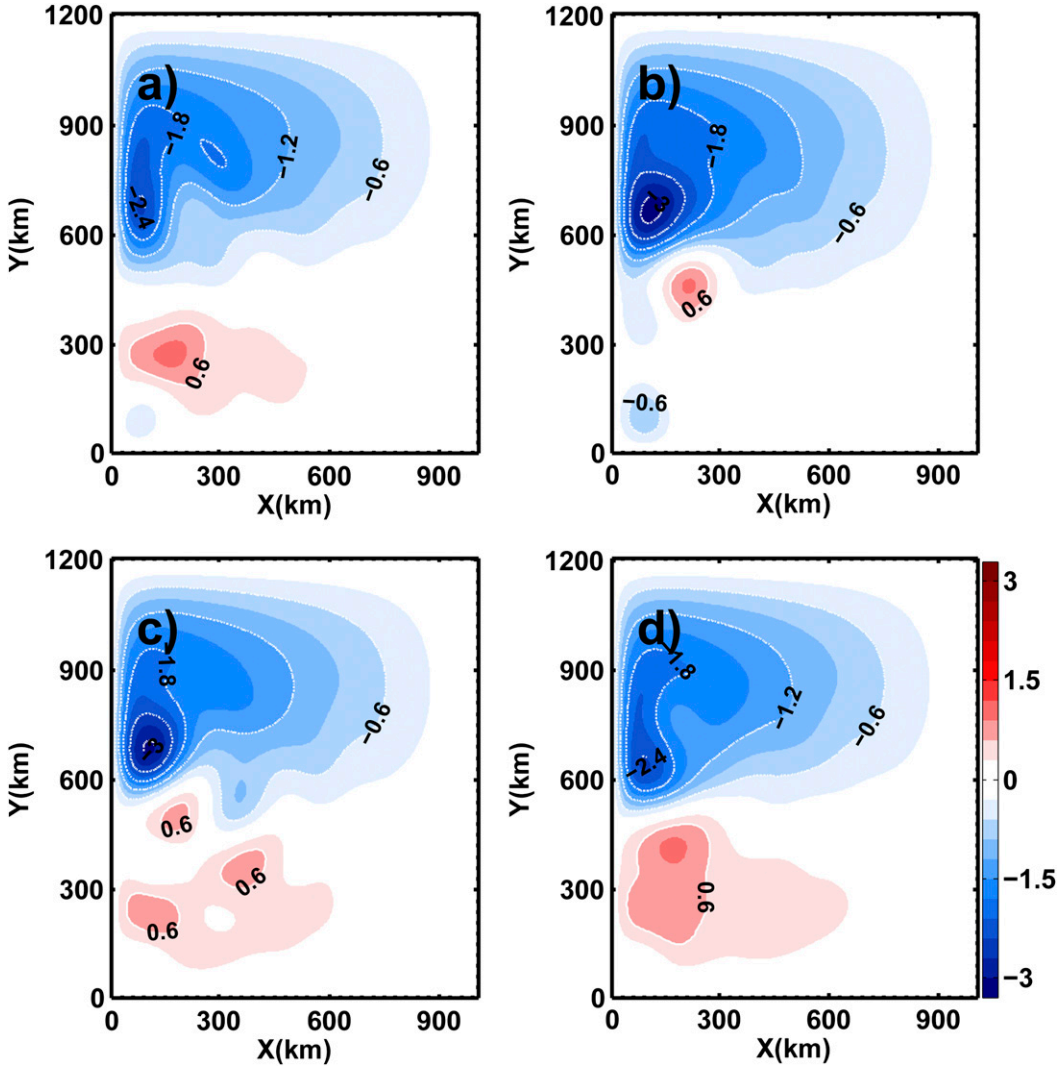

FIG. 11. As in Fig. 9, but for *W*-forcing case.

d. Dynamics of the interannual mode under seasonal forcing

According to the previous discussion, the intrinsic variability of the SCS in the W_{winter}-forcing case is dominated by linear Rossby wave adjustment, while it is found to be driven by nonlinear terms associated with intergyre PV flux in the W_{summer}-forcing case. As the interannual variability in the *W*-forcing case shows a similar pattern and frequency to that in the W_{summer}-forcing case, we analyze its dynamics by calculating PV balances for different stages of the cycle. Figure 11 shows the key states associated with the interannual variability with the sequence of transitions A → D → B → C → A according to the definitions in the previous section. In state A (Fig. 11a), the circulation is characterized by a weaker double-gyre system relative to that in Fig. 2b. The transition process from A to D (Fig. 11d) describes the northward migration of the SG and slight intensification of the northern gyre (NG). Then, the SG vanishes in state B, while the NG keeps on strengthening and intrudes into the southern basin (Fig. 11b). When it reaches its southernmost position, the NG begins to retreat northward while the SG starts to establish (Fig. 11c). Finally, the development of the SG and the weakening of the NG characterize the transition to state A, and then the cycle repeats itself. To further demonstrate this cycle, phase space consisting of their corresponding PCs (PC1 and PC2) is shown (Fig. 12), following Wheeler and Hendon (2004). It is diagnosed that most of the sequential points trace anticlockwise circles around the origin, which signifies that the cycle is robust.

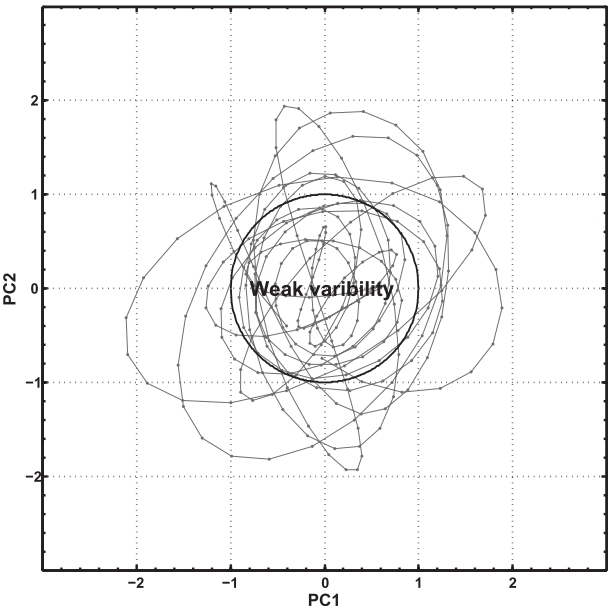

FIG. 12. (PC1, PC2) phase space. The region of weak variability is labeled. Here, monthly mean values of PC1 and PC2 are used.

Different from the W_{summer}-forcing case, we define the location of the EJ that separates the basin based on the maximum velocity near the midbasin rather than zero line of dynamical streamfunction because the anticyclonic gyre only exists in summer. Considering this, we will focus on PV balance of the NG in this section. By this definition, the EJ shows a significant seasonal meridional shifting with its time-mean position to the north of the mean zero wind curl line (Fig. 13a). Along the EJ, two maximum velocities can be found that capture the western boundary current and the standing meandering of the NG (Fig. 13b). The lengths of the EJ for all seasons are more than 200 km (judged by 0.1 m s^{-1}), indicating that the midbasin-located EJ is perennial.

Table 3 summarizes the PV budget in the NG, which is characterized by the balance between wind forcing and the diffusive boundary flux for all stages. Compared with those in the W_{summer}-forcing case, variances of all terms are larger, which is mainly caused by the strong seasonal evolution of the SCS circulation. Intergyre eddy PV flux is only the third major contributor in the balance, but its role in driving the interannual variability mode is crucial, as indicated by its larger variance compared to the other three terms. According to Berloff et al. (2007b), it is regulated by the strength of the EJ associated with the eddy rectification effect, which describes enhancement of the upper-ocean EJ and its adjacent recirculation zones due to the eddy. To understand the evolution of intergyre flux $\boldsymbol{v}'q'$ in driving the interannual mode, its distribution along the jet during the cycle is plotted (Fig. 14). The mean intergyre PV flux is negative (Fig. 14a) with most of this exchange taking place near the western boundary (0–150 km) where both the eddy kinetic energy and the intergyre PV gradient are maximal. In the interior of the basin, intergyre fluxes tend to be small but positive, which is a characteristic feature associated with the eddy rectification process (Fig. 14a). The intergyre PV transition from state A to D is characterized by slightly enhanced negative values near the western boundary and positive values to the east (Fig. 14b), which can be attributed to the activated instability associated with the western boundary current and the EJ. In the transition from state D to B (Fig. 14c), the negative intergyre flux is found to be inhibited near the western boundary (0–100 km) of the basin, which is because of the enhanced intergyre PV contrast induced by the intensification of the NG, whereas the basin-averaged flux almost remains the same from B to C (Fig. 14d). After that, the intergyre flux intensifies again along with the weakening of the EJ caused by the reduced wind PV input, and then the cycle repeats.

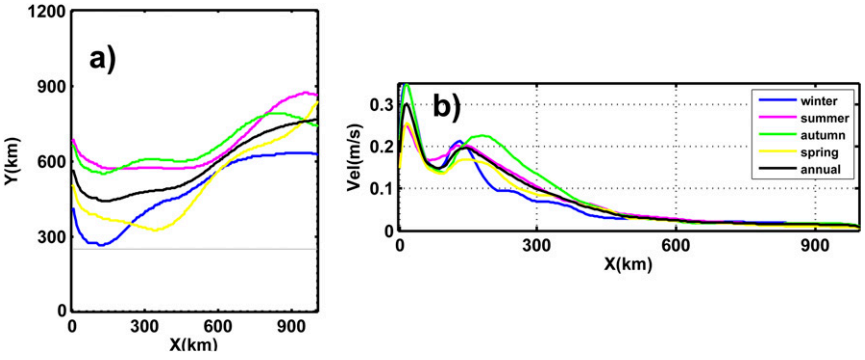

FIG. 13. (a) Positions of the EJ in four seasons. (b) Velocity as a function of x along the EJ. Straight line in (a) indicates the annual-mean zero wind forcing line.

TABLE 3. Potential vorticity balances (10^{-4} m^2 s^{-2}) for the upper-layer SCS of NG in *W*-forcing case.

	A	D	B	C	Mean	Std
Wind input	1156	1156	1185	1112	1153	30
Diffusive boundary flux	−820	−852	−873	−850	−848	22
Eddy intergyre flux	−220	−218	−140	−123	−175	60
Diffusive intergyre flux	−164	−146	−110	−118	−134	25
Total	−48	−60	62	21	−4	57

Figure 15 shows the spatial distribution of P and R associated with the leading EOF pair. For the first mode, the energy exchange P (Fig. 15a) depicts the maximum in the EJ extension area, while P associated with the second mode is characterized by positive values at the EJ origin (Fig. 15c). Both of them show similar patterns to those in the W_{summer}-forcing case, indicating the same dynamics in driving their interannual modes. Compared with P, the magnitude of R is much smaller with significant values near the western boundary. The area integral of P is positive, whereas the area integral of R is close to zero, which has an indication that barotropic instability is the primary mechanism destabilizing the flow.

According to the previous discussion, the interannual variability of the SCS in the *W*-forcing case is driven by the anomalous intergyre PV flux, which is same as the W_{summer}-forcing case. However, compared to that in the W_{summer}-forcing case, the EJ under seasonal forcing is much weaker and shorter. This is the reason why interannual variability in the *W*-forcing case depicts smaller amplitude and smaller energy exchange. In the next section, we will test the robustness of this variability by adopting the parameter sensitivity study.

e. *Parameter sensitivity study*

Many parameters in our numerical experiments have an influence on the interannual variability. It is necessary to explore the flow behavior through parameter space. Here, the main uncertain parameters are the magnitude of wind-forcing W, the reduced gravity g', the horizontal eddy viscosity A_H, and the boundary condition parameter α. We compute several additional solutions differing from the reference solution in terms of these parameters to validate the generality of the flow behavior and the variance found in the reference solution. The annual-mean, upper-layer circulations are presented in Fig. 16, and the frequencies of the leading EOF pairs for sensitivity experiments are listed in Table 4.

Figures 16a and 16b show the annual-mean solutions driven by 0.8*W* and 1.6*W*. Both of these two solutions depict similar patterns to those in Fig. 2c and are dominated by tripolar and dipolar EOF modes on an interannual time scale. As Table 4 shows, the frequency of the variability for these two additional solutions are around 0.66 yr^{-1}, which is very close to that of reference solution, suggesting the robustness of the interannual modes. In addition, by successively varying the wind forcing over a wider range (1*W*–2.5*W*), the changing of frequency is also detected but no significant trend is

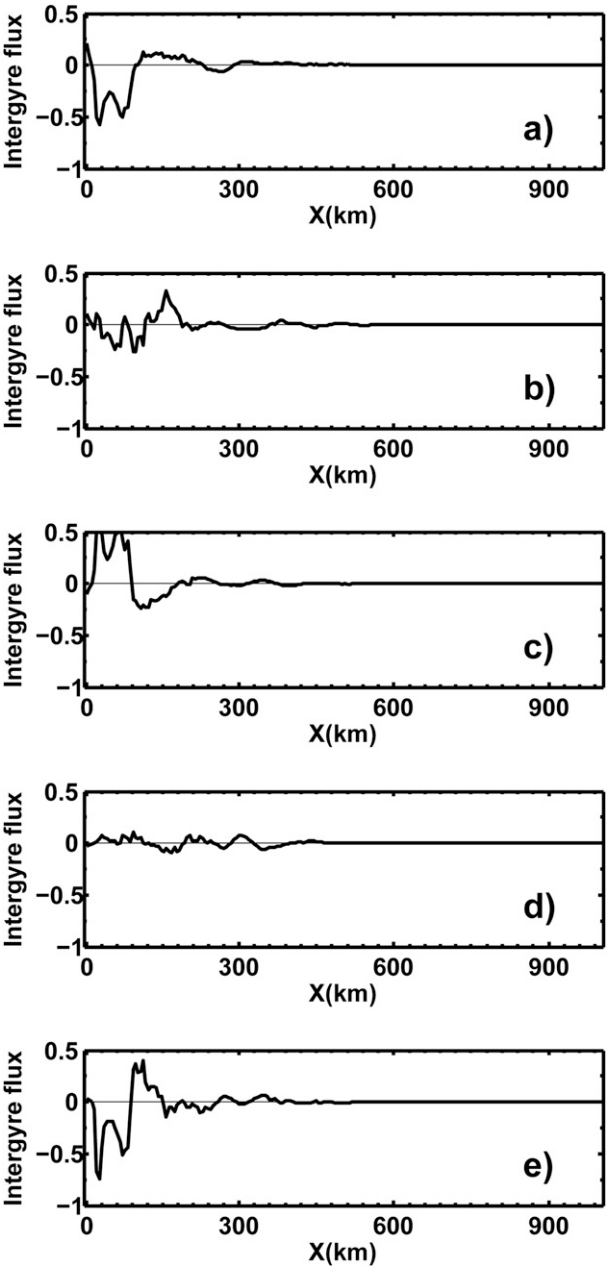

FIG. 14. Intergyre PV fluxes (10^{-6} m s^{-2}) for the upper layer in *W*-forcing case. (a) Time-mean flux and 2 times the difference between the fluxes in states: (b) D and A, (c) B and D, (d) C and B, and (e) A and C.

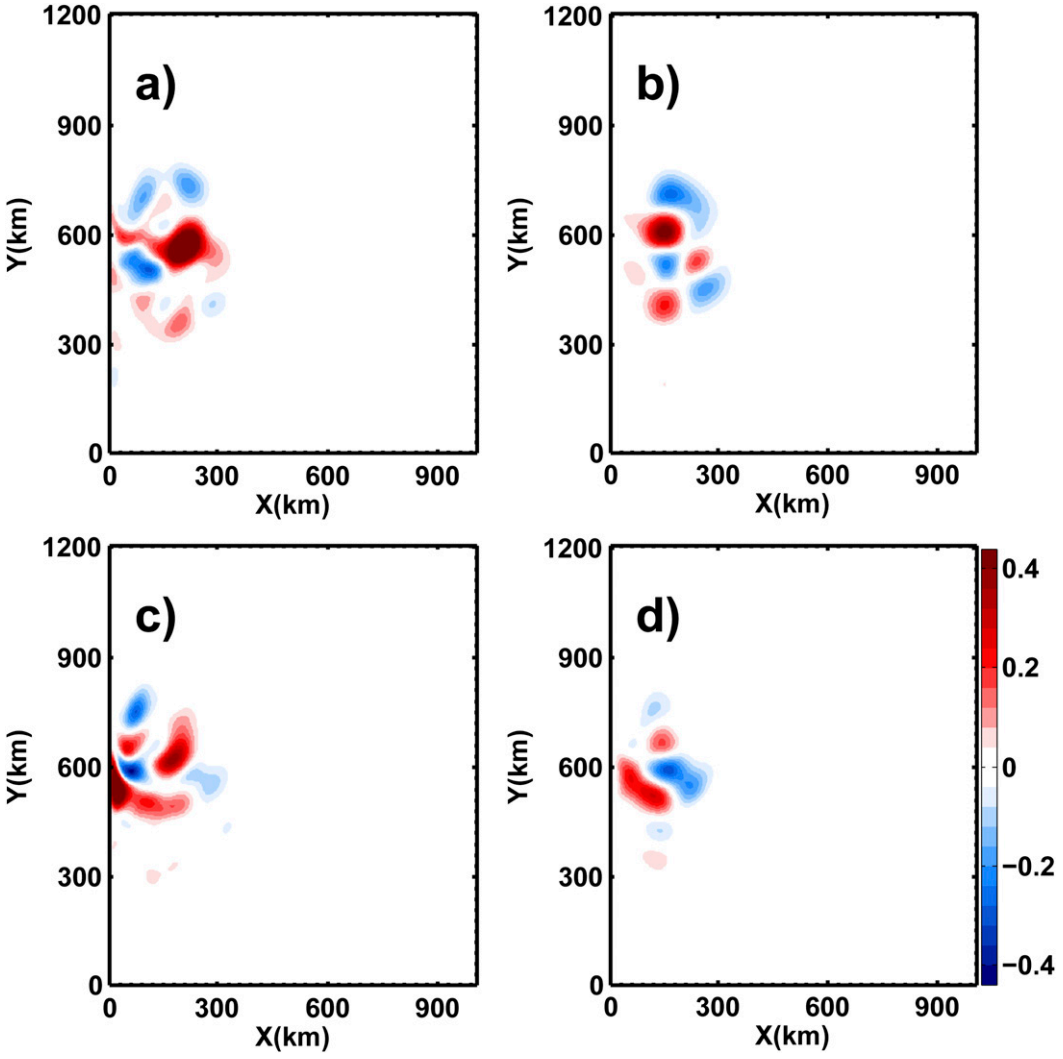

FIG. 15. As in Fig. 10, but for W-forcing case. Units here are $10^{-10}\,m^2\,s^{-3}$.

found. This is different from the behavior shown in Berloff et al. (2007a), indicating the role of seasonally varying wind in influencing the interannual cycle. Sensitivity to the stratification is explored by varying g'. It is found that the time-mean upper-layer transport is insensitive to the stratification (Figs. 16c,d), while the frequency decreases systematically with increasing g'. Figures 16e and 16f are the results of sensitivity experiments varying the eddy viscosity A_H. Similar to the reference solution, the two solutions under lower ($100\,m^2\,s^{-1}$) and higher ($200\,m^2\,s^{-1}$) A_H are both characterized by winterlike patterns with maximum transport around 2.5 Sv. EOF analysis for the I band is carried out for the two solutions and similar modes as the reference solution variance are found. Spectral analyses show that the frequencies of interannual modes for these two additional solutions are 0.6/0.66 and $0.54\,yr^{-1}$, which are also very close to that of the reference solution. These features indicate that the behavior of the interannual variability seems insensitive to the eddy viscosity in the regime discussed above.

By keeping values of other parameters constant and varying α, it is found that the time-mean flow is strongly sensitive to the partial-slip boundary condition (Figs. 16g–j). When α is close to the reference solution ($\alpha = 0.05$, $0.2\,km^{-1}$; Figs. 16h,i), the variability is also characterized by tripolar and dipolar EOF modes with similar frequencies to the reference solution. But the feature of variability is not generic when the partial-slip parameter approaches its limits. For $\alpha = 0$ (free-slip boundary; Fig. 16j), the annual-mean field is characterized by a cyclonic gyre in the southern basin caused by zero viscous stress on the boundary without interannual modes in the midbasin. In the other limit case, $\alpha \to \infty$ (no-slip

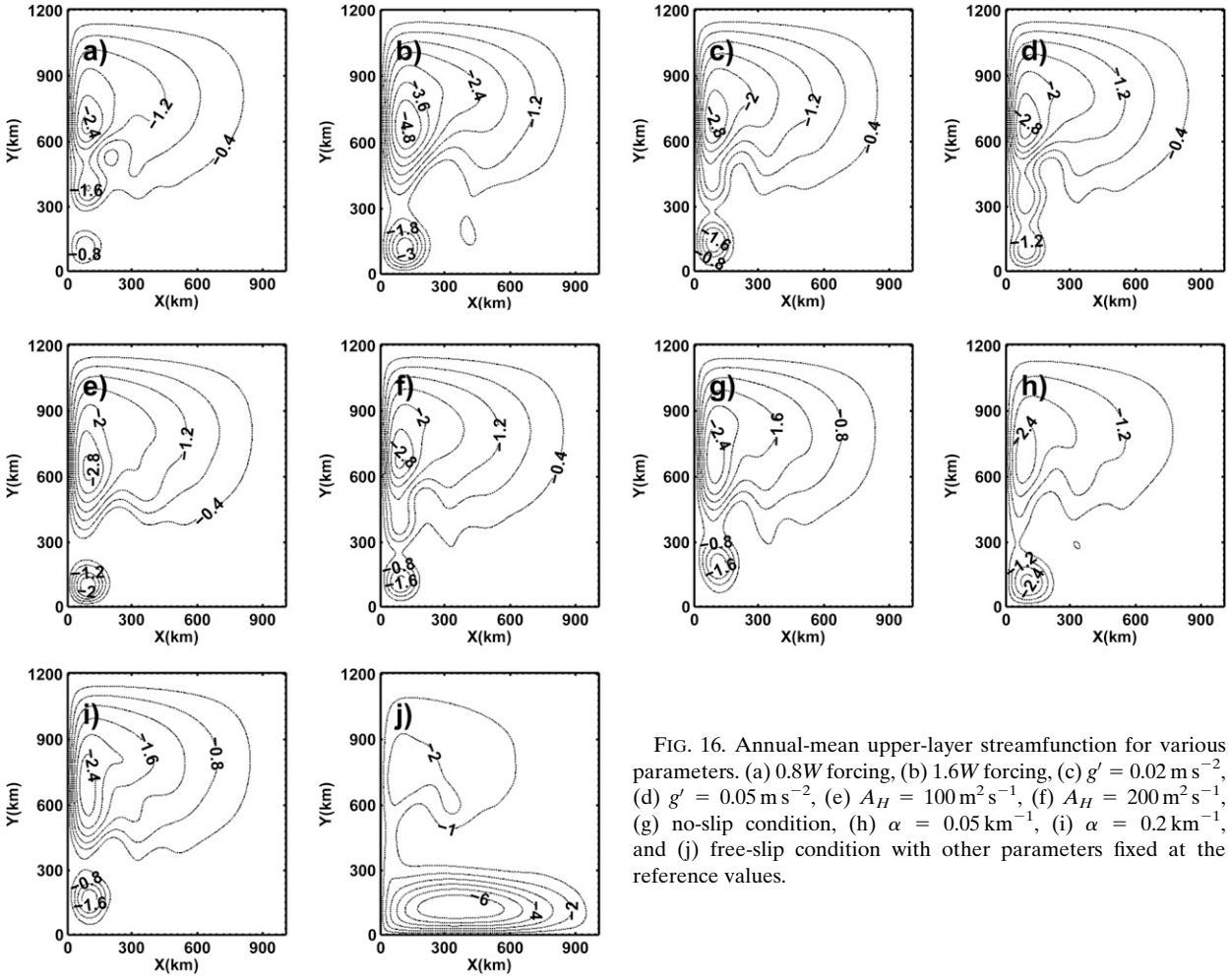

FIG. 16. Annual-mean upper-layer streamfunction for various parameters. (a) $0.8W$ forcing, (b) $1.6W$ forcing, (c) $g' = 0.02\,\mathrm{m\,s^{-2}}$, (d) $g' = 0.05\,\mathrm{m\,s^{-2}}$, (e) $A_H = 100\,\mathrm{m^2\,s^{-1}}$, (f) $A_H = 200\,\mathrm{m^2\,s^{-1}}$, (g) no-slip condition, (h) $\alpha = 0.05\,\mathrm{km^{-1}}$, (i) $\alpha = 0.2\,\mathrm{km^{-1}}$, and (j) free-slip condition with other parameters fixed at the reference values.

boundary; Fig. 16g), although the same modes can be found, the frequency is much smaller because of the extreme viscous stress on the boundary.

f. Interannual variability in OGCM

To further validate the EOF modes in the QG model, we perform EOF analysis on I-band SSH products from OFES model data with patterns and associated frequencies shown in Fig. 17. The second EOF mode (24.5%) shows a similar pattern and frequency with the second mode derived from the QG model, depicting a tripolar structure symmetric with 13°N where the EJ locates (not shown). While the fourth mode (10.4%) is similar to the first mode in the QG model, it is characterized by a dipolar pattern with a frequency around 0.6–0.8 $\mathrm{yr^{-1}}$, which suggests that the interannual modes in QG model are robust. Compared to these two modes, the first (29.4%) and third (12.1%) mode capture high values along the northern continental shelf and the Vietnam coast. This indicates the role of other factors, such as topography and the shape of the basin, in regulating the interannual evolution in the SCS that will be addressed in the future.

4. Discussion and conclusions

Based on a QG model, the interannual variability of circulation driven by seasonal wind in the upper-layer

TABLE 4. Frequencies ($\mathrm{yr^{-1}}$) of tripolar and dipolar modes for the sensitivity experiments.

Sensitivity parameter	Tripolar mode	Dipolar mode
$0.8W$ forcing	0.78	0.66
$1.6W$ forcing	0.66	0.66
$g' = 0.02\,\mathrm{m\,s^{-2}}$	0.84	0.78
$g' = 0.05\,\mathrm{m\,s^{-2}}$	0.48	0.48
$A_H = 100\,\mathrm{m^2\,s^{-1}}$	0.6	0.66
$A_H = 200\,\mathrm{m^2\,s^{-1}}$	0.54	0.54
Nonslip condition	0.4	0.4
$\alpha = 0.05\,\mathrm{km^{-1}}$	0.66	0.7
$\alpha = 0.2\,\mathrm{km^{-1}}$	0.48	0.52

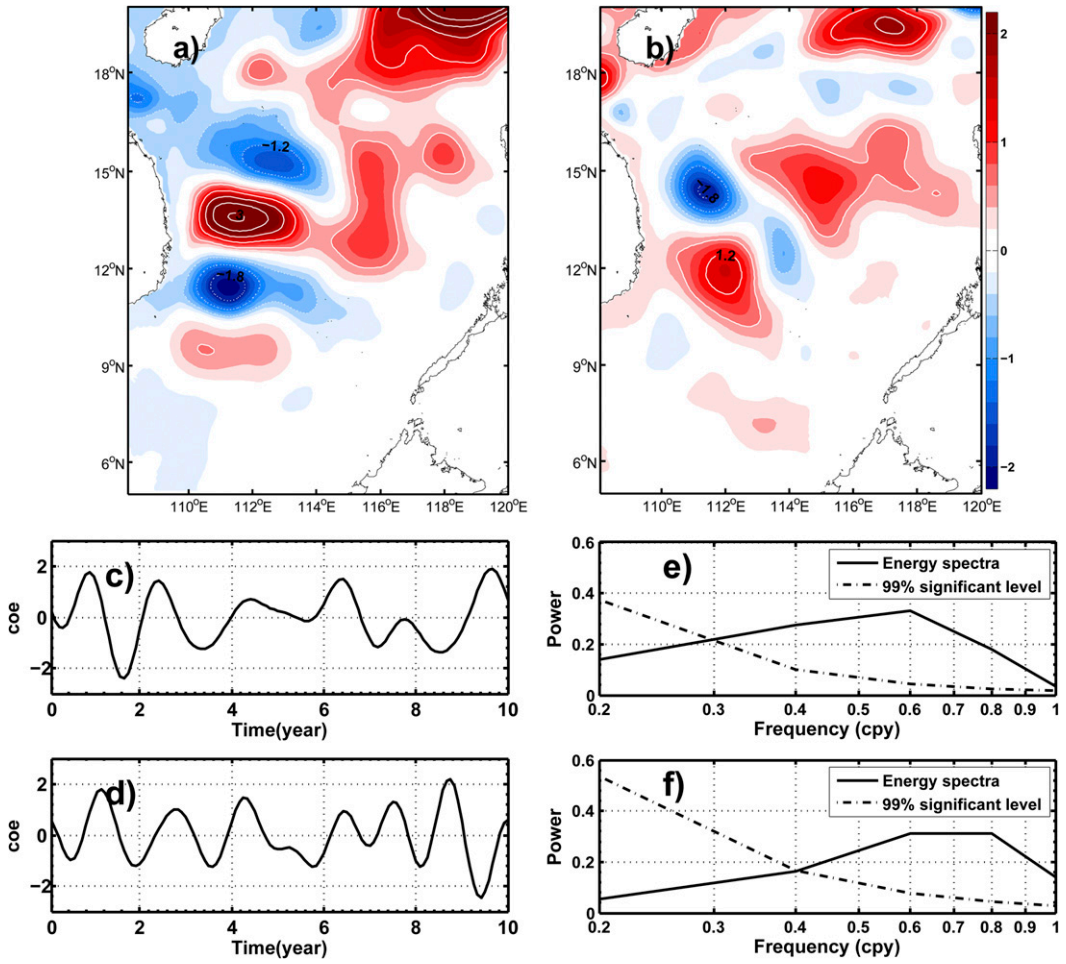

FIG. 17. (a) Second and (b) fourth mode of EOF for I-band SSH (cm) from OFES. (c),(d) Their corresponding PCs with (e),(f) energy spectra.

SCS is investigated in this study. The first two interannual modes are characterized by dipolar and tripolar structures with frequency $0.6\,\mathrm{yr}^{-1}$. Time-lag correlation analysis suggests a periodic cycle associated with them. Further analysis indicates that interannual evolution of the upper-layer SCS is dominated by the double-gyre system in the summer season. To explain this phenomenon, two more experiments, that is, the W_{summer}-forcing case and W_{winter}-forcing case, are performed to detect intrinsic variability of the SCS. It is found that the intrinsic variability in the W_{winter}-forcing case is dominated by linear Rossby wave adjustment, while it is driven by wind forcing and intergyre eddy PV flux associated with barotropic instability in the W_{summer}-forcing case. As the interannual variability in W-forcing case shows similar pattern and frequency with that in W_{summer}-forcing case, we analyze its dynamics by calculating PV balances for different stages of the cycle. Results show that the interannual variability is driven by the intergyre PV flux. Energy analysis further indicates that interannual modes attain energy mainly through barotropic instability.

Besides the upper-layer, the interannual variability in the bottom layer is also detected. As the absence of the direct wind forcing, transport is significantly smaller than that in the upper layer. The leading EOF pair for I-band flow accounts for 35.8% and 19.9% of the total variance, respectively. Both of these two modes depict zonal wavelike patterns (not shown) and significant correlation with their upper-ocean counterparts with 4-month lag, indicating the role of eddy-driven downgradient mixing in driving the variability in the bottom.

Recent studies have suggested that intrinsic variability plays an important role in regulating the low-frequency variability of gyre circulation in the open ocean (e.g., Qiu and Miao 2000; Penduff et al. 2011; Pierini et al. 2014). To assess its importance in the SCS, we compute

several additional solutions driven by the wind-involving interannual component:

$$W_E = W + 0.3\cos(\Omega_E t)W. \quad (10)$$

Here, the dominant interannual atmospheric component, which is associated with ENSO, describes the strengthening/weakening of the seasonal cycle. We explore the changing of interannual variability by systematically varying Ω_E over a wide range (0.1–0.9 yr^{-1}). It is found that for most Ω_E, the first EOF mode is characterized by a single-gyre pattern similar to previous studies (Wu and Chang 2005; Y. G. Wang et al. 2006), capturing the ocean response to interannual forcing. Moreover, interannual variability in the SCS is also detected based on observations and ocean models driven by the actual wind field, but no dipolar and tripolar modes are found. This suggests that the interannual variability of the SCS is mainly induced by the variability of wind forcing rather than intrinsic ocean dynamics.

It should also be noted that more studies are required to clarify the role of topography and basin shape in regulating the interannual variability of the SCS circulation. The Kuroshio intrusion may also affect the SCS circulation (Hu et al. 2000; Liu et al. 2008), which is not analyzed in the current study. Furthermore, the dynamics responsible for the time scale of the variability should be investigated in detail in the future. The result of this study will be a step toward understanding the interannual variability of circulation in the SCS.

Acknowledgments. This research is supported by National Major Research Plan of Global Change (2013CB956201). We thank Dr. Liping Zhang and Dr. Daling Li Yi for helpful advice. Comments from the anonymous reviewers are greatly appreciated.

REFERENCES

Berloff, P., 2005: On the rectification of randomly forced flows. *J. Mar. Res.,* **63,** 497–527, doi:10.1357/0022240054307894.

——, and S. Meacham, 1997: The dynamics of an equivalent-barotropic model of the wind-driven circulation. *J. Mar. Res.,* **55,** 407–451, doi:10.1357/0022240973224319.

——, and ——, 1998: The dynamics of a simple baroclinic model of the wind-driven circulation. *J. Phys. Oceanogr.,* **28,** 361–388, doi:10.1175/1520-0485(1998)028<0361:TDOASB>2.0.CO;2.

——, and J. McWilliams, 1999: Large-scale, low-frequency variability in wind-driven ocean gyres. *J. Phys. Oceanogr.,* **29,** 1925–1949, doi:10.1175/1520-0485(1999)029<1925:LSLFVI>2.0.CO;2.

——, A. Mc C. Hogg, and W. Dewar, 2007a: The turbulent oscillator: A mechanism of low-frequency variability of the wind-driven ocean gyres. *J. Phys. Oceanogr.,* **37,** 2363–2386, doi:10.1175/JPO3118.1.

——, S. Kravtsov, W. Dewar, and J. McWilliams, 2007b: Ocean eddy dynamics in a coupled ocean–atmosphere model. *J. Phys. Oceanogr.,* **37,** 1103–1121, doi:10.1175/JPO3041.1.

Bryan, K., 1963: A numerical investigation of a nonlinear model of a wind-driven ocean. *J. Atmos. Sci.,* **20,** 594–606, doi:10.1175/1520-0469(1963)020<0594:ANIOAN>2.0.CO;2.

Carton, J. A., G. Chepurin, X. Cao, and B. S. Giese, 2000: A Simple Ocean Data Assimilation analysis of the global upper ocean 1950–95. Part I: Methodology. *J. Phys. Oceanogr.,* **30,** 294–309, doi:10.1175/1520-0485(2000)030<0294:ASODAA>2.0.CO;2.

——, B. S. Giese, and S. A. Grodsky, 2005: Sea level warming of the oceans in the Simple Ocean Data Assimilation (SODA) ocean reanalysis. *J. Geophys. Res.,* **110,** C090006, doi:10.1029/2004JC002817.

Cessi, P., and G. R. Ierley, 1995: Symmetry-breaking multiple equilibria in quasigeostrophic, wind-driven flows. *J. Phys. Oceanogr.,* **25,** 1196–1205, doi:10.1175/1520-0485(1995)025<1196:SBMEIQ>2.0.CO;2.

——, and S. Louazel, 2001: Decadal oceanic response to stochastic wind forcing. *J. Phys. Oceanogr.,* **31,** 3020–3029, doi:10.1175/1520-0485(2001)031<3020:DORTSW>2.0.CO;2.

Chang, C., H. Hsu, C. Wu, and W. Sheu, 2008: Interannual mode of sea level in the South China Sea and the roles of El Niño and El Niño Modoki. *Geophys. Res. Lett.,* **35,** L03601, doi:10.1029/2007GL032562.

Chen, C., and G. Wang, 2014: Interannual variability of the eastward current in the western South China Sea associated with the summer Asian monsoon. *J. Geophys. Res. Oceans,* **119,** 5745–5754, doi:10.1002/2014JC010309.

Chu, P., N. Edmons, and C. Fan, 1999: Dynamical mechanisms for the South China Sea seasonal circulation and thermohaline variabilities. *J. Phys. Oceanogr.,* **29,** 2971–2989, doi:10.1175/1520-0485(1999)029<2971:DMFTSC>2.0.CO;2.

Dewar, W., 2003: Nonlinear midlatitude ocean adjustment. *J. Phys. Oceanogr.,* **33,** 1057–1081, doi:10.1175/1520-0485(2003)033<1057:NMOA>2.0.CO;2.

Dijkstra, H. A., and M. Ghil, 2005: Low-frequency variability of the large scale ocean circulation: A dynamical approach. *Rev. Geophys.,* **43,** RG3002, doi:10.1029/2002RG000122.

Fang, G., W. Fang, Y. Fang, and K. Wang, 1998: A survey of studies on the South China Sea upper ocean circulation. *Acta Oceanogr. Taiwan.,* **37,** 1–16.

——, H. Chen, Z. Wei, Y. Wang, X. Wang, and C. Li, 2006: Trends and interannual variability of the South China Sea surface winds, surface height, and surface temperature in the recent decade. *J. Geophys. Res.,* **111,** C11S16, doi:10.1029/2005JC003276.

Haidvogel, D., J. McWilliams, and P. Gent, 1992: Boundary current separation in a quasigeostrophic, eddy-resolving ocean circulation model. *J. Phys. Oceanogr.,* **22,** 882–902, doi:10.1175/1520-0485(1992)022<0882:BCSIAQ>2.0.CO;2.

Holland, W., 1978: The role of mesoscale eddies in the general circulation of the ocean—Numerical experiments using a wind-driven quasigeostrophic model. *J. Phys. Oceanogr.,* **8,** 363–392, doi:10.1175/1520-0485(1978)008<0363:TROMEI>2.0.CO;2.

Hu, J., H. Kawamura, H. Hong, and Y. Qi, 2000: A review on the currents in the South China Sea: Seasonal circulation, South China Sea warm current and Kuroshio intrusion. *J. Oceanogr.,* **56,** 607–624, doi:10.1023/A:1011117531252.

Jiang, S., F. Jin, and M. Ghil, 1995: Multiple equilibria and aperiodic solutions in a wind-driven double gyre, shallow water model. *J. Phys. Oceanogr.,* **25,** 764–786, doi:10.1175/1520-0485(1995)025<0764:MEPAAS>2.0.CO;2.

Li, Y., W. Han, J. L. Wilkin, W. G. Zhang, H. Arango, J. Zavala-Garay, J. Levin, and F. S. Castruccio, 2014: Interannual variability of the surface summertime eastward jet in the South China Sea. *J. Geophys. Res. Oceans,* **119,** 7205–7228, doi:10.1002/2014JC010206.

Liu, Q., X. Jiang, S. Xie, and W. T. Liu, 2004: A gap in the Indo-Pacific warm pool over the South China Sea in boreal winter: Seasonal development and interannual variability. *J. Geophys. Res.,* **109,** C07012, doi:10.1029/2003JC002179.

——, A. Kaneko, and J. Su, 2008: Recent progress in studies of the South China Sea circulation. *J. Oceanogr.,* **64,** 753–762, doi:10.1007/s10872-008-0063-8.

——, M. Feng, and D. Wang, 2011: ENSO-induced interannual variability in the southeastern South China Sea. *J. Oceanogr.,* **67,** 127–133, doi:10.1007/s10872-011-0002-y.

Liu, Z., H. Yang, and Q. Liu, 2001: Regional dynamics of seasonal variability in the South China Sea. *J. Phys. Oceanogr.,* **31,** 272–284, doi:10.1175/1520-0485(2001)031<0272:RDOSVI>2.0.CO;2.

McCalpin, J. D., and D. B. Haidvogel, 1996: Phenomenology of the low-frequency variability in a reduced gravity quasigeostrophic double-gyre model. *J. Phys. Oceanogr.,* **26,** 739–752, doi:10.1175/1520-0485(1996)026<0739:POTLFV>2.0.CO;2.

McWilliams, J., 1977: A note on a consistent quasigeostrophic model in a multiply connected domain. *Dyn. Atmos. Oceans,* **1,** 427–441, doi:10.1016/0377-0265(77)90002-1.

Meacham, S., and P. Berloff, 1997a: Barotropic, wind-driven circulation in a small basin. *J. Mar. Res.,* **55,** 523–563, doi:10.1357/0022240973224364.

——, and ——, 1997b: Instabilities of a steady, barotropic, wind driven circulation. *J. Mar. Res.,* **55,** 885–913, doi:10.1357/0022240973224166.

Mu, L., L. Zhong, L. Hua, and J. Song, 2011: Low-frequency variability of a semi-closed sea induced by the circulation in an adjacent ocean in a wind-driven, quasi-geostrophic, eddy-resolving simulation. *Ocean Dyn.,* **61,** 1459–1473, doi:10.1007/s10236-011-0443-2.

Pedlosky, J., 1987: *Geophysical Fluid Dynamics.* 2nd ed. Springer-Verlag, 710 pp.

Penduff, T., M. Juza, B. Barnier, J. Zika, W. Dewar, A. Treguier, J. Molines, and N. Audiffren, 2011: Sea level expression of intrinsic and forced ocean variabilities at interannual time scales. *J. Climate,* **24,** 5652–5670, doi:10.1175/JCLI-D-11-00077.1.

Pierini, S., H. Dijkstra, and A. Riccio, 2009: A nonlinear theory of the Kuroshio extension bimodality. *J. Phys. Oceanogr.,* **39,** 2212–2229, doi:10.1175/2009JPO4181.1.

——, H. Dijkstrab, and M. Mu, 2014: Intrinsic low-frequency variability and predictability of the Kuroshio Current and of its extension. *Adv. Oceanogr. Limnol.,* **5,** 79–122, doi:10.1080/19475721.2014.962091.

Primeau, F., 2002: Multiple equilibria and low-frequency variability of the wind-driven ocean circulation. *J. Phys. Oceanogr.,* **32,** 2236–2256, doi:10.1175/1520-0485(2002)032<2236:MEALFV>2.0.CO;2.

Qiu, B., and W. Miao, 2000: Kuroshio path variations south of Japan: Bimodality as a self-sustained internal oscillation. *J. Phys. Oceanogr.,* **30,** 2124–2137, doi:10.1175/1520-0485(2000)030<2124:KPVSOJ>2.0.CO;2.

Sasaki, H., and Coauthors, 2004: A series of eddy-resolving ocean simulations in the world ocean: OFES (OGCM for the Earth Simulator) project. *Proc. Oceans '04 MTS/IEEE Techno-Ocean '04,* Kobe, Japan, IEEE, 1535–1541, doi:10.1109/OCEANS.2004.1406350.

——, M. Nonaka, Y. Masumoto, Y. Sasai, H. Uehara, and H. Sakuma, 2007: An eddy-resolving hindcast simulation of the quasi-global ocean from 1950 to 2003 on the Earth Simulator. *High Resolution Numerical Modeling of the Atmosphere and Ocean,* K. Hamilton and W. Ohfuchi, Eds., Springer, 157–185.

Simonnet, E., M. Ghil, K. Ide, R. Temam, and S. Wang, 2003: Low-frequency variability in shallow-water models of the wind-driven ocean circulation. Part I: Steady-state solutions. *J. Phys. Oceanogr.,* **33,** 712–728, doi:10.1175/1520-0485(2003)33<712:LVISMO>2.0.CO;2.

Spydell, M., and P. Cessi, 2003: Baroclinic modes in a two-layer basin. *J. Phys. Oceanogr.,* **33,** 610–622, doi:10.1175/1520-0485(2003)033<0610:BMIATL>2.0.CO;2.

Sun, S., L. Wu, and B. Qiu, 2013: Response of the inertial recirculation to intensified stratification in a two-layer quasi-geostrophic ocean circulation model. *J. Phys. Oceanogr.,* **43,** 1254–1269, doi:10.1175/JPO-D-12-0111.1.

Wang, C., W. Wang, D. Wang, and Q. Wang, 2006: Interannual variability of the South China Sea associated with El Niño. *J. Geophys. Res.,* **111,** C03023, doi:10.1029/2005JC003333.

Wang, D., W. Wang, P. Shi, P. Guo, and Z. Gan, 2003: Establishment and adjustment of monsoon-driven circulation in the South China Sea. *Sci. China Ser. D,* **46,** 173–181, doi:10.1360/03yd9016.

——, and Coauthors, 2013: Progress of regional oceanography study associated with western boundary current in the South China Sea. *Chin. Sci. Bull.,* **58,** 1205–1215, doi:10.1007/s11434-012-5663-4.

Wang, G. H., D. Chen, and J. L. Su, 2006: Generation and life cycle of the dipole in the South China Sea summer circulation. *J. Geophys. Res.,* **111,** C06002, doi:10.1029/2005JC003314.

Wang, Y. G., G. H. Fang, Z. X. Wei, F. L. Qiao, and H. Y. Chen, 2006: Interannual variation of the South China Sea circulation and its relation to El Niño, as seen from a variable grid global ocean model. *J. Geophys. Res.,* **111,** C11S14, doi:10.1029/2005JC003269.

Wheeler, M. C., and H. H. Hendon, 2004: An all-season real-time multivariate MJO index: Development of an index for monitoring and prediction. *Mon. Wea. Rev.,* **132,** 1917–1932, doi:10.1175/1520-0493(2004)132<1917:AARMMI>2.0.CO;2.

Wu, C., and C. Chang, 2005: Interannual variability of the South China Sea in a data assimilation model. *Geophys. Res. Lett.,* **32,** L17611, doi:10.1029/2005GL023798.

——, P. Shaw, and S. Chao, 1998: Seasonal and interannual variation of the velocity field of the South China Sea. *J. Oceanogr.,* **54,** 361–372, doi:10.1007/BF02742620.

Wyrtki, K., 1961: *Physical Oceanography of the Southeast Asian Waters.* Naga Rep., Vol. 2, Scripps Institute of Oceanography, 195 pp.

Xie, S., Q. Xie, D. Wang, and W. T. Liu, 2003: Summer upwelling in the South China Sea and its role in regional climate variations. *J. Geophys. Res.,* **108,** 3261, doi:10.1029/2003JC001867.

Yang, H., and L. Wu, 2012: Trends of upper-layer circulation in the South China Sea during 1959–2008. *J. Geophys. Res.,* **117,** C08037, doi:10.1029/2012JC008068.